Quantitative analysis of the synergistic effect of Au nanoparticles on SnO2-rGO nanocomposites for room temperature hydrogen sensing

Journal:	*Physical Chemistry Chemical Physics*
Manuscript ID	CP-ART-11-2020-005701.R2
Article Type:	Paper
Date Submitted by the Author:	12-Jan-2021
Complete List of Authors:	Wang, Yale; University of Wisconsin Milwaukee, Pu, Haihui; University of Chicago, Pritzker School of Molecular Engineering Lu, Ganhua; University of Wisconsin-Milwaukee, Mechanical Engineering Sui, Xiaoyu; University of Chicago, Pritzker School of Molecular Engineering Chen, Junhong; University of Chicago, Pritzker School of Molecular Engineering

Quantitative analysis of the synergistic effect of Au nanoparticles on SnO_2-rGO nanocomposites for room temperature hydrogen sensing

Yale Wang,[1] Haihui Pu,[1] Ganhua Lu,[1] Xiaoyu Sui,[1] Junhong Chen[1,2,3*]

[1] Department of Mechanical Engineering, University of Wisconsin-Milwaukee, 3200 North Cramer Street, Milwaukee, WI 53211, USA

[2]Current address: Pritzker School of Molecular Engineering, University of Chicago, 5640 S. Ellis Ave, Chicago, Illinois 60637, USA.

[3]Current address: Chemical Sciences and Engineering Division, Physical Sciences and Engineering Directorate, Argonne National Laboratory, 9700 S. Cass Ave, Lemont, Illinois 60439, USA.

Abstract

Hydrogen detection devices based on gold-tin oxide/reduced graphene oxide (Au-SnO_2/rGO) nanohybrids were fabricated by combining a hydrothermal method with sputter coating. The gas sensing performance of the Au-SnO_2/rGO sensor was investigated under different concentrations of hydrogen from 0.04% to 1% at room temperature, which indicated a notable sensitive response even for 0.04% hydrogen. The activation energies of hydrogen adsorption/desorption were extracted via Arrhenius analysis which revealed the acceleration effect of gold dopants. This acceleration led to a faster response and recovery during hydrogen sensing. The activation energy analysis provided a more comprehensive understanding on the gas sensing mechanism. A hydrogen detection handheld device is demonstrated by integrating the sensor chip with a portable digital meter for direct readout of test results.

1. Introduction

Hydrogen (H_2) has been considered and investigated as one of the most promising sustainable fuels since it produces no air pollutants in fuel cells. However, hydrogen is very flammable and could lead to an explosion at a high concentration (4%) in air.[1] As hydrogen is colorless, odorless, and highly flammable under ambient conditions, it must be reliably monitored in real time during its production, delivery, storage, and utilization.

The composites based on rGO indicated great potential in wide applications due to their superior electrical properties.[2] Graphene has been widely reported as a promising gas sensing material due to the extreme single gas molecule sensitivity, large surface-to-volume ratio, and excellent electronic signal transduction property (high carrier mobility and high signal-to-noise ratio).[3] However, lack of selectivity and poor sensitivity to hydrogen limit its application for hydrogen sensing.[4] As is well known, the sensing performance of graphene could be improved through functionalization with metal oxides or noble metals.[5] Tin oxide (SnO_2) is one of the most widely investigated metal oxides for gas sensing applications owing to its high response, low cost, and good stability.[6-9] The SnO_2 nanocrystals-rGO sensing platform reported in our previous work demonstrated advantages such as tunable sensing performance and room temperature operation.[10] Since SnO_2-rGO based sensing material still suffers from cross-sensitivity to NO_2,[7] CO[11] and H_2S,[8] further surface modification to the SnO_2-rGO platform is needed to improve the selectivity. Noble metals, especially palladium (Pd)[12-14 15, 16] and platinum (Pt),[17, 18] were widely used in H_2 sensors due to their high solubility and ability to dissociate hydrogen molecules. However, a highly enhanced sensitivity due to activated hydrogen dissociation also leads to poor sensor recovery. The practical balance between sensing and recovery performances is an ongoing pursuit.

Gold is another noble metal dopant for gas sensing which is more abundant than platinum on earth with a lower cost than palladium.[19-25] Ci and his group investigated the ammonia gas sensing property of the rGO/SnO_2@Au heterostructure devices prepared via magnetron sputtering.[26] The enhanced sensing performance was ascribed to the synergistic effect provided by heterointerfaces between Au/SnO_2 and SnO_2/rGO. However, the related sensing mechanism still needs to be further supported by in-situ characterization or kinetic analysis. Zhang et al. synthesized the Au-loaded SnO_2 composite by a hydrothermal method and investigated the hydrogen sensing properties of the sensor based on the composite.[19] The Au-loaded SnO_2 composite showed ~~a~~ high sensitivity, a low detection limit, and excellent selectivity for H_2 at an elevated temperature of 250 °C to activate the adsorption process. However, the elevated operating temperature leads to high power consumption and reduced sensor stability. In this case, sensors with reliable hydrogen sensing performance at room temperature are desirable. Therefore, it is promising to combine the gold dopant with the SnO_2-rGO sensing template to achieve desirable hydrogen sensing performance at room temperature.

2. Experimental

2.1 Fabrication of sensors

SnO_2/rGO nanohybrids were prepared first. In a typical synthesis, GO (8 mg) was dispersed in DI water (10 mL), in which 45 µl of HCl (37%) was added. Then $SnCl_2{\bullet}2H_2O$ (50 mg) was dissolved in the DI water (10 mL) with 30 mins stirring at 90 °C. Afterward, the aqueous solution of $SnCl_2{\bullet}2H_2O$ was added ~~in~~to the GO dispersion under magnetic stirring at 90 °C for 1 h. After cooling down to room temperature, the SnO_2-rGO nanohybrids were washed with DI water ~~for~~ several times and dried at 60 °C overnight. Finally, SnO_2-rGO powders were obtained.

Au doped SnO_2/rGO nanohybrids were prepared through the sputter coating method. 20 mg SnO_2-rGO powders were dissolved in 50 ml DI water under ultrasonication. Then, 2 µl of dispersion was drop-casted on the interdigitated electrodes, which was reported previously.[27] After drying at room temperature, Au nanoparticles were deposited onto the surface of these sensors using a sputter coater (K550X, Quorum Technologies). The sputtering current was 20 mA and the sputtering time was varied from 3 to 12 s for different gold area densities. These sensors were annealed at 200 °C for 1 h in Ar flow (1 lpm) to improve the contact between the nanohybrids and the gold electrodes. Pure rGO and SnO_2-rGO sensors were also prepared as control samples.

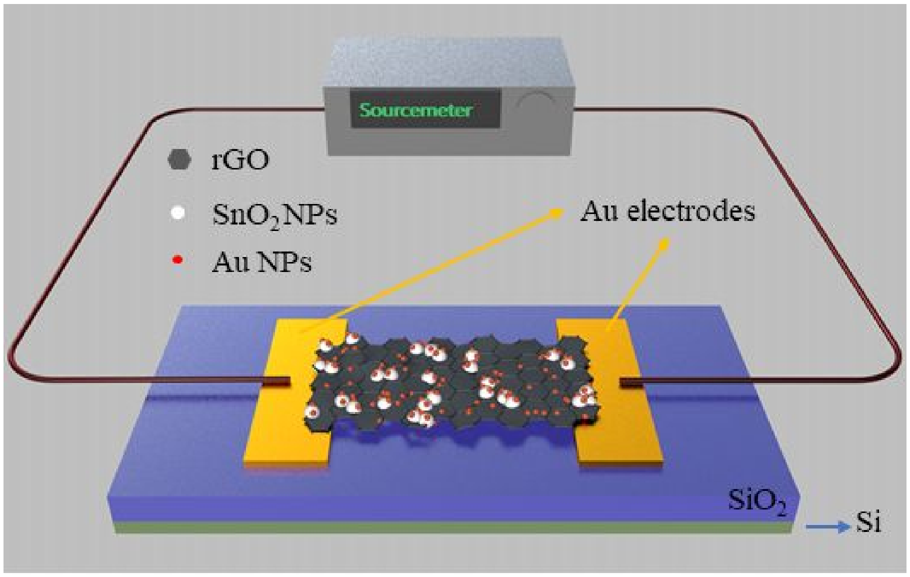

Figure 1. Schematic of the Au-SnO_2/rGO sensor device and measurement system.

2.2 Characterization and gas sensing test

The morphologies of the materials were observed by a Hitachi (S4800) field-emission scanning electron microscopy (FE-SEM). The energy-dispersive X-ray spectroscopy (EDS) line scanning data were obtained using a Bruker detector on the Hitachi S-4800 FE-SEM. X-ray diffraction

(Bruker D8 Discover X-ray diffractometer) was performed to identify the crystalline phases. X-ray photoelectron spectroscopy (XPS) was conducted by using VG ESCA 2000 with an Mg Kα as source and the C1s peak at 284.5 eV as an internal standard.

Figure 1 shows a schematic of the Au-SnO_2/rGO sensor device and the circuit for electrical measurements. A typical gas sensing test cycle had three steps. The first step was the introduction of clean carrier gas into the sensing chamber and was used to obtain a baseline measurement. The typical preset time for this step was 10 minutes or until the baseline became stable. The second step was the addition of various target gases being injected through the flowmeter into the test chamber with the same flow rate as the first step to generate the sensing signal. The exposure time for the target gas was 5 minutes. Finally, the third step involved the target gas is turned off and a 100% composition of the carrier gas being introduced again for sensor recovery. The third step lasts for at least 10 minutes.

3. Results and discussion

3.1 Characterization

The crystallization of the SnO_2/rGO nanocomposite was examined by X-ray diffraction (XRD). The XRD patterns (Figure 2c) of the SnO_2/rGO nanocomposite display clear reflections from the (110), (101), (211) and (112) planes of rutile SnO_2, indicating the formation of SnO_2 crystals.[28]

Figure S1 shows the XRD pattern of the Au doped SnO_2-rGO nanocomposite. There are no visible peaks of gold due to its relatively small loading.

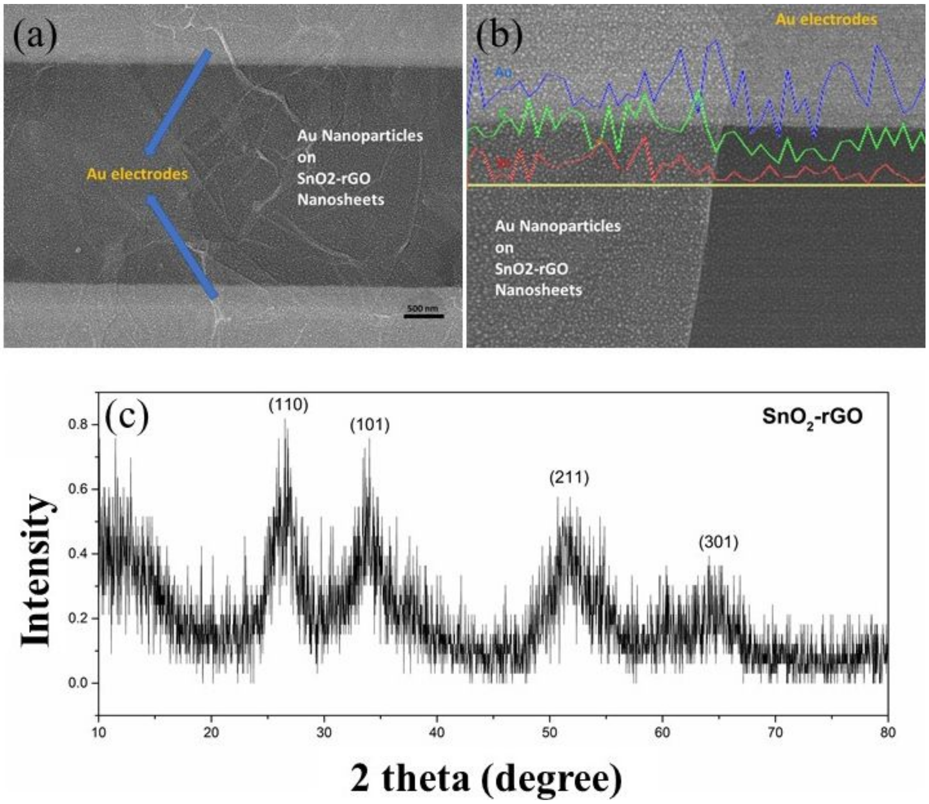

Figure 2 (a) SEM image of Au-SnO_2/rGO sensor chip. (b) Line scan EDX data combined with SEM image of the Au-SnO_2/rGO sensor. (c) XRD pattern of SnO_2-rGO nanohybrids.

Scanning electron microscopy (SEM) was used to analyze the morphology of Au-SnO_2/rGO nanohybrids and the sensor chip (Figure 2a). The rGO nanosheets bridging two gold electrodes were modified with well-dispersed SnO_2 and Au nanoparticles on the surface (Figure 2a and S1). The existence of Sn and Au elements could be verified through the line scan (Figure 2b) of Energy-dispersive X-ray (EDX) analysis. X-ray photoelectron spectroscopy (XPS) was conducted to examine the elemental composition and chemical states of the species in the GO and Au-SnO_2/rGO nanohybrids. The thickness of the sputtered Au layer was characterized using SEM and EDX with a tilted sample (Figure S3). There is no continuous Au layer formed after the 12-second gold sputtering. The thickness of the gold clusters is around a hundred nanometers, as shown in Figure S3.

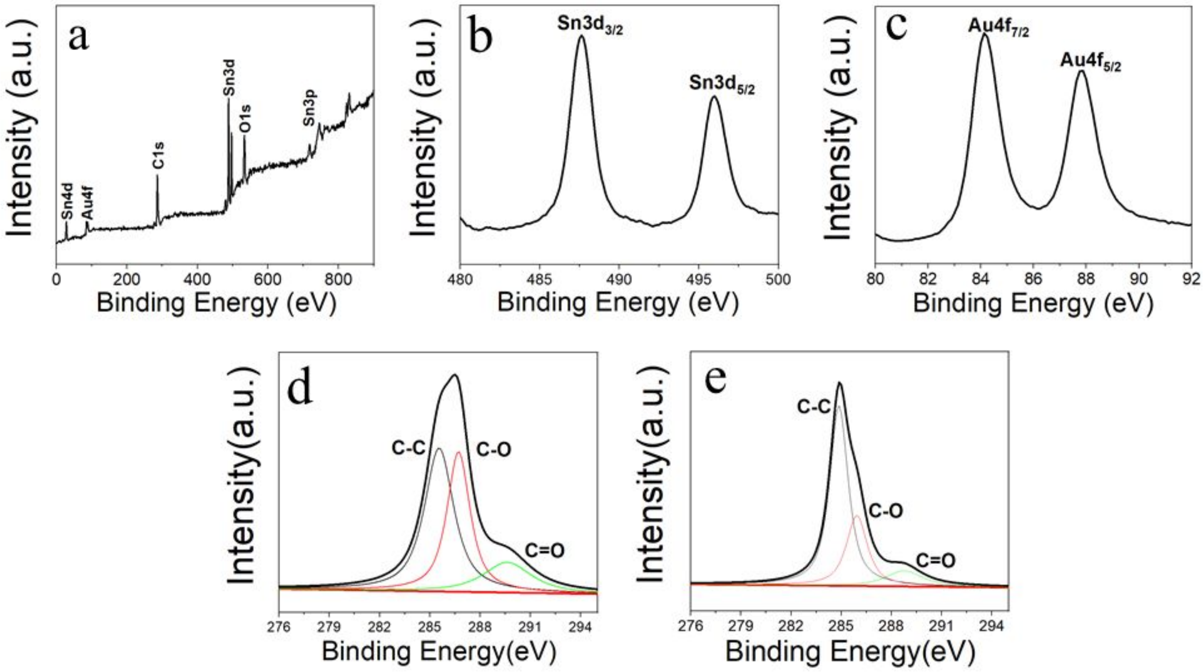

Figure 3. XPS spectra of a) Au-SnO_2/rGO nanohybrids. b) Sn 3d and c) Au 4f spectra of the Au-SnO_2/rGO nanohybrids. C 1s of d) the GO and e) the Au-SnO_2/rGO nanohybrids.

The wide-survey XPS spectrum (Figure 3a) of the Au-SnO_2/rGO nanohybrids reveals the existence of Au, Sn, O, and C elements. Figure 2b indicates two characteristic peaks at 496.0 eV and 487.5 eV, which are attributed to the binding energy of Sn $3d_{5/2}$ and Sn $3d_{3/2}$, respectively.[29] The XPS spectrum of Au (Figure 3c) presents two main peaks at 84.1 eV and 87.8 eV, which are related to $Au4f_{7/2}$ and $Au4f_{5/2}$, respectively, suggesting the existence of metallic Au on the surface.[30] XPS C1s spectrum has been reported as an effective method to estimate the reduction level of graphene oxide.[31] The C1s spectra of GO (Figure 2d) and Au-SnO_2-rGO (Figure 3e) all consist of three characteristic peaks, corresponding to C-C, C-O, and C=O groups.[32] The intensities of C-O (285.9 eV) and C=O (288.8 eV) in Figure 2e are all reduced compared to the intensities of the relevant peaks from GO C1s spectra. This reduction reveals the reduced amount of oxygen from GO to Au-SnO_2/rGO nanohybrids, which agrees well with Raman analysis (Fig. S4).

3.2 Gas sensing performance

To unveil the effect of gold nanoparticle doping on hydrogen gas sensing, we investigated the sensor response towards hydrogen gas with or without dopants in a laboratory-built testing system.

Here, we define the sensitivity as Response (%) = $[(I_g - I_a)/I_a \times 100]$, where I_g is the current in the presence of H_2 and I_a is the base current in the air. The small enhancement (1.5%) of hydrogen detection through SnO_2 nanoparticles decoration is indicated in Figure 4a. This is due to the small coverage of chemisorbed oxygen on the SnO_2 surface at room temperature.[17] Figure 4b shows the typical response curves of rGO and Au-rGO to 1% H_2. Pure rGO sensors exhibit a weak response (2.5%) to 1% H_2 which is consistent with the previous report.[4] rGO modified with sputtered Au nanoparticles shows improved sensitivity and partial recovery, most likely due to the higher-energy binding sites provided by Au nanoparticles; full recovery was not achieved in 10 minutes under room temperature.

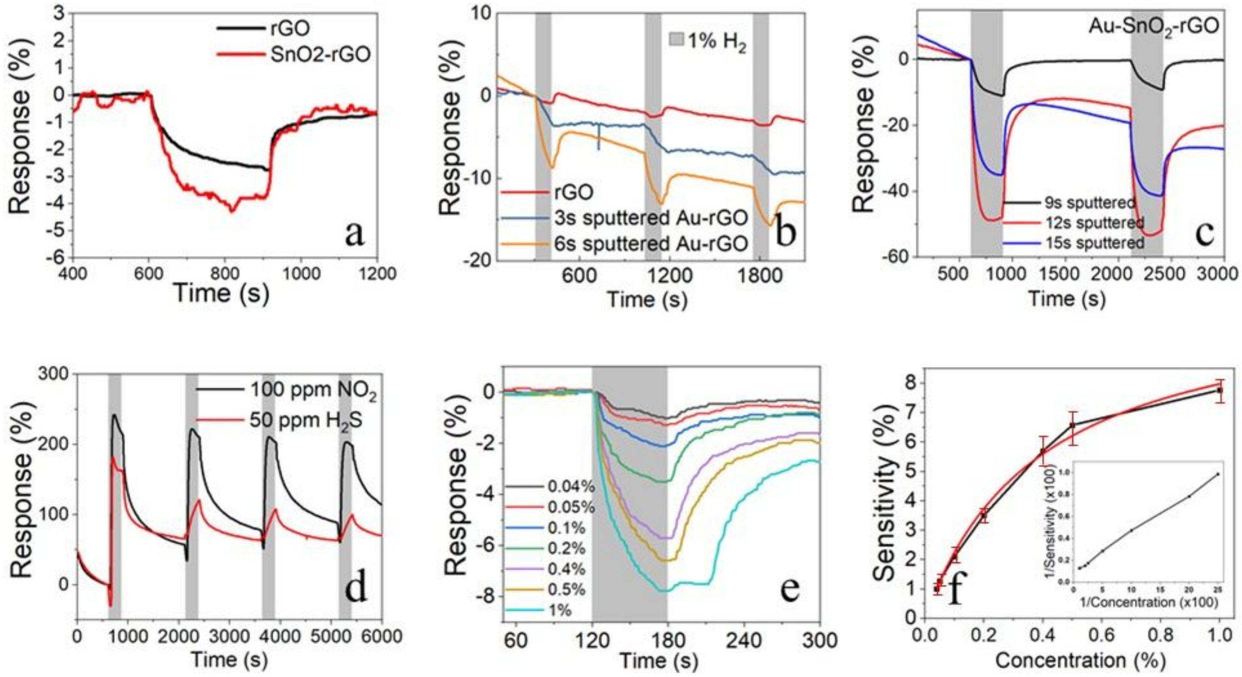

Figure 4. Responses to 1% H_2 of a) rGO and SnO_2-rGO. b) rGO and Au-rGO. c) Au-SnO_2/rGO nanohybrids with different sputtered gold thickness. d) dynamic response curves of 12s sputtered Au-SnO_2/rGO to 100 ppm NO_2 and 50 ppm H_2S. e) dynamic response curves of 12s sputtered Au-SnO_2/rGO to H_2 with varying concentrations from 0.04% to 1% in 1 min. f) Calibration curves of 1 nm Au-SnO_2/rGO sensors to H_2 gas.

Figure 4b-c shows the dynamic response of Au-SnO_2/rGO nanohybrids to 1% H_2 with different Au loading amounts related to different sputtering time length. Figure S2 indicates the good uniformity of the gold nanoparticles on the silicon wafer through sputtering. The quantitative EDS analysis results of the surface elements are shown in Table S1. The sensitivity reached 47% after baseline subtraction for 12s sputtered Au loaded SnO_2-rGO sensors in 5 minutes of hydrogen exposure at 21.5 °C (RT). The good repeatability of this device is evidenced by the multicycle sensing (Figure 4c). The sensing responses to 100 ppm NO_2 and 50 ppm H_2S (Figure 4d) showed a quick decay in sensitivity and deactivation after several cycles, which is likely due to the strong binding of NO_2/H_2S molecules that consumes the chemisorbed oxygen and leads to the poisoning effect on the sensing surface.[33-35] The poisoning effect may be related to the drained out of the chemisorbed oxygen or binding sites after several sensing cycles. The hydrogen concentration-related dynamic response curves and the calibration curves are indicated in Figure 4e-f.

$$\text{Sensitivity} = \frac{\text{a}}{1 + \frac{\text{b}}{\text{Concentration}}}$$

Figure 4f is well fitted by the Langmuir isotherm[36], where a is a constant equal to 11.1353 without unit and b is another constant equal to 0.3955 has the same unit as the concentration (%). This can be explained from the relationship between the surface coverage and gas partial pressure in Langmuir isotherm, which has been confirmed by the linear fitting of 1/Sensitivity vs. 1/Concentration shown in Figure 4f inset. The sensitivity variation within the same batch of devices was illustrated by the standard deviation for each concentration (Figure 4f). The device's variation was around ±20% at high concentrations (0.2% - 1%). For lower concentrations (≤0.1%), the variation decreased to less than ±10%, which suggests good reproducibility of the devices.

The excellent sensing performance is competitive when compared with other reported room temperature hydrogen sensors, as summarized in Supplementary Table S2. The ratio of the response to our optimal sensor response time is around 0.78% per second, which is higher than all other reported noble metal doped heterostructure sensors except the Pd-MLGN sensor. However, our sensor indicates better recovery performance (~180 s) compared with the Pd-MLGN sensor (300 s) at room temperature. The outstanding balance between the response and the recovery performance makes our sensor more practical.

3.3 Gas sensing mechanism

To better understand the sensing mechanism, the transfer properties are analyzed with respect to the hydrogen adsorption. The p-type behavior suggests that the dominant charge carriers in the Au-SnO_2/rGO nanocomposite are holes. Both SnO_2 and Au nanoparticles could be regarded as the catalytic materials in hydrogen sensing under different sensing steps. Since SnO_2 is an n-type material and rGO is a p-type material, p-n junctions are formed at the interface. The electrons flow from SnO_2 to rGO nanosheets due to the smaller work function of SnO_2 nanoparticles compared with rGO (Fig. 5).[37, 38] The larger work function differences between Au NPs and SnO_2 NPs compared to SnO_2 NPs and rGO lead to the back flow of electrons from rGO to Au, resulting in the recovery of the conductivity of Au-SnO_2/rGO nanocomposite in the I-V curve (Fig. S5a). The I-V curves for Au doped SnO_2-rGO sensors with different gold sputtering duration is shown in Figure S5b. The significant current increase the 12-second gold sputtering suggests the efficient charge transfer within optimal sensor devices.

The electrons on the surface of Au NPs and SnO_2 accelerated the adsorption of oxygen in ambient air. O_2^- could be formed on the SnO_2 surface at room temperature. [39, 40]

$$\mathbf{O_2 + e \rightarrow O_2^- (ads)} \qquad \textbf{(1)}$$

Au nanoparticles on the SnO_2 and rGO surfaces could also act as catalytic sites which accelerate the dissociation of H_2 and O_2 molecules.[19]

$$\mathbf{H_2 \rightarrow 2H(ads)} \qquad \textbf{(2)}$$

The dissociated hydrogen can migrate and combine with the adsorbed oxygen to form water molecules with the overall reactions as,

$$\mathbf{O_2^- (ads) + 4H(ads) \rightarrow 2H_2O + e^-} \qquad \textbf{(3)}$$

$$\mathbf{O_2^- + 2H_2 \rightarrow 2H_2O + e} \qquad \textbf{(4)}$$

The accelerating effect of Au nanoparticles on hydrogen dissociation can give rise to the enhanced response but poor recovery of Au-rGO sensors (Fig. 4b). The better recovery of Au-SnO_2/rGO sensors indicate that the loaded Au nanoparticles on SnO_2 is more related to oxygen spillover[41] rather than hydrogen dissociation, and thus the reactions (2) and (3) should be present in a small proportion compared to (4). The dissociation of hydrogen leads to partial non-recovery at room temperature due to the higher binding energy (Fig. 4c). However, the synergistic effect among rGO, SnO_2 and Au nanoparticles promotes the great balance between the sensitivity and recovery performance of sensors.

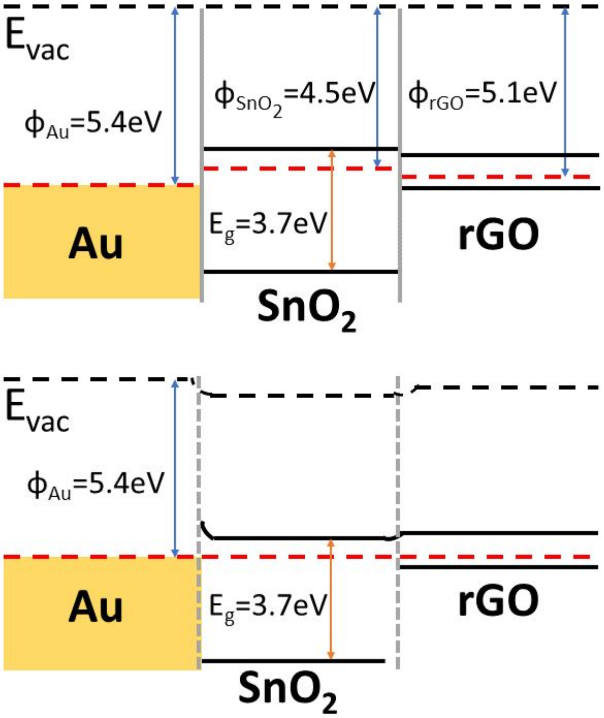

Figure 5. Schematic band diagrams of Au-SnO_2/rGO sensors (top figure) with the heterojunction formation at the interfaces (bottom figure).

The enhanced sensing performance facilitated by Au NPs was generally attributed to the catalytic effect of Au NPs on the hydrogen molecular dissociation and the hydrogen spillover effect. However, the acceleration effect of Au NPs on hydrogen adsorption/desorption was rarely investigated kinematically. Arrhenius plots are often used to analyze the effect of temperature on the rates of chemical reactions and determine the related activation energies. Ural and his group extracted the hydrogen desorption activation energy from Pd nanoparticles to reveal the dominant recovery mechanism through Arrhenius plot analysis.[12] Weiller et al. determined NO_2 sensor recovery activation energy using the initial slope of the recovery cycle and further understood the binding sites on reduced graphene oxides.[42] In this report, the hydrogen adsorption/desorption kinetics were extracted and analyzed through a temperature-dependence study and the Arrhenius plot analysis, which refines the understanding of the observed acceleration effect of gold nanoparticles on hydrogen sensing.

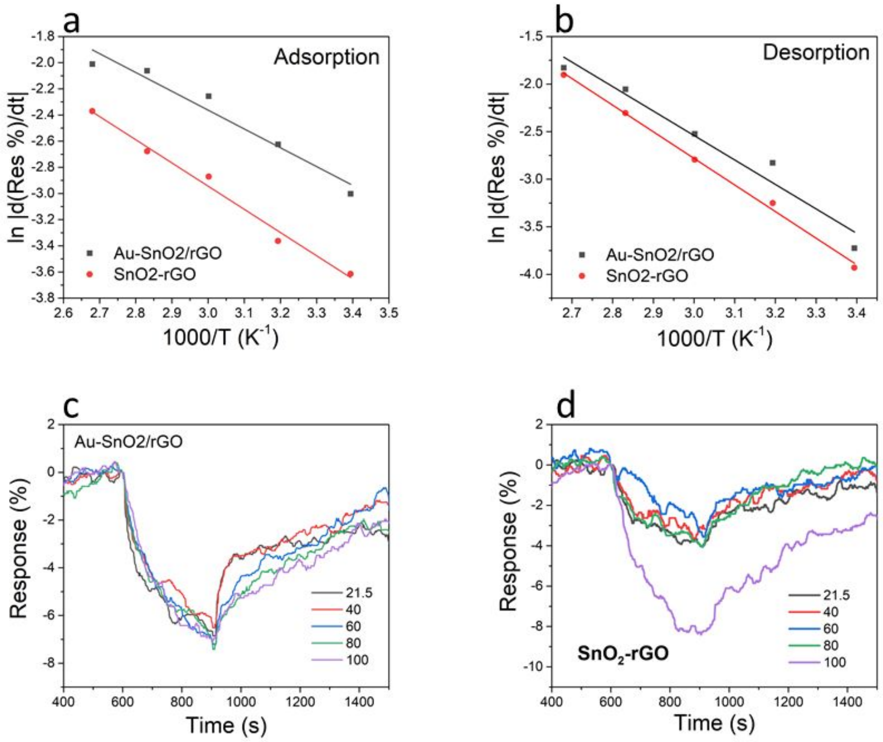

Figure 6. a-b) The Arrhenius plot of ln |d (Res%)/dt| determined from the initial slope of the recovery cycle. Dynamic response curves of c) Au-SnO_2/rGO and d) SnO_2-rGO sensors to 1% H_2 in the temperature range 21.5-100 ℃.

To verify this, the temperature-dependent sensing test was conducted to analyze the adsorption and desorption kinetics quantitatively.[43] Figure 6a-b shows the Arrhenius plot of the rate of relative current change determined from the initial slope of the response and recovery cycle from room temperature 21.5 °C (RT) to 100 °C. The activation energies, E_a, for hydrogen adsorption are extracted as 152.9 meV (SnO_2-rGO) and 124.0 meV (Au-SnO_2-rGO). The E_a of SnO_2-rGO and Au-SnO_2-rGO for hydrogen desorption are also extracted as 241.0 meV and 221.6 meV, respectively. The sensors with loaded Au nanoparticles indicate reduced activation energies in both hydrogen adsorption and desorption. The reduction in the activation energy for desorption leads to a shorter recovery time (~600 s) than that of SnO_2-rGO (>600 s) at varying temperatures.

A hydrogen detection prototype handheld device (Figure S6) was further developed. Based on the calibration data (Fig. 4f), a portable digital meter was programmed. The digital meter was tested against 0.04%, 0.1%, 0.4%, and 1% hydrogen diluted with compressed air in the gas chamber. The real responses of the handheld device are very close to the standard values (Fig. S6) with errors within ±20%.

4. Conclusion

In summary, the Au-SnO_2/rGO ternary nanohybrids were designed with improved room temperature H_2 sensing performance. The sputtered Au nanoparticles enhanced both sensitivity and recovery of the SnO_2-rGO template. Such enhancement was attributed to the increased surface area and the oxygen spillover effect of loaded Au nanoparticles. The catalytic effect of Au nanoparticles for hydrogen adsorption and desorption was then revealed through the temperature-dependent sensing test and Arrhenius analysis. Better balance between sensitivity and recovery can be further achieved in the future by tuning the deposition conditions of Au nanoparticles. A prototype handheld device based on the Au-SnO_2/rGO composites was finally developed for hydrogen detection. This prototype device demonstrates the potential for real-time hydrogen monitoring. The availability of such sensors will contribute to promoting a sustainable hydrogen economy, protecting public safety, and enhancing the lead-acid battery safety in a wide range of applications.

Acknowledgments

The authors would like to acknowledge financial support from the National Science Foundation (IIP-1701203). The material characterization was performed at the Bioscience Electron Microscope Facility and the Advanced Analysis Facility at the University of Wisconsin–Milwaukee.

Competing Financial Interests

J.C. has financial interests in NanoAffix Science LLC, which did not fund this work. All other authors declare no competing financial interests.

Data Availability Statement

The data that supports the findings of this study are available within the article and its supplementary material.

References**Uncategorized References**

1. I. Sayago, E. Terrado, E. Lafuente, M. C. Horrillo, W. K. Maser, A. M. Benito, R. Navarro, E. P. Urriolabeitia, M. T. Martinez and J. Gutierrez, *Synthetic Met*, 2005, **148**, 15-19.
2. J. Feng, Z. Zhang, L. Ci, W. Zhai, Q. Ai and S. Xiong, *Journal of Power Sources*, 2015, **287**, 177-183.
3. F. Schedin, A. K. Geim, S. V. Morozov, E. W. Hill, P. Blake, M. I. Katsnelson and K. S. Novoselov, *Nat Mater*, 2007, **6**, 652-655.
4. R. S. Sundaram, C. Gómez-Navarro, K. Balasubramanian, M. Burghard and K. Kern, *Advanced Materials*, 2008, **20**, 3050-3053.
5. R. Malik, V. K. Tomer, Y. K. Mishra and L. Lin, *Applied Physics Reviews*, 2020, **7**.
6. H. Huang, H. Gong, C. L. Chow, J. Guo, T. J. White, M. S. Tse and O. K. Tan, *Advanced Functional Materials*, 2011, **21**, 2680-2686.
7. H. Zhang, J. Feng, T. Fei, S. Liu and T. Zhang, *Sensors and Actuators B: Chemical*, 2014, **190**, 472-478.
8. Z. Song, Z. Wei, B. Wang, Z. Luo, S. Xu, W. Zhang, H. Yu, M. Li, Z. Huang, J. Zang, F. Yi and H. Liu, *Chemistry of Materials*, 2016, **28**, 1205-1212.
9. I. Paulowicz, V. Hrkac, S. Kaps, V. Cretu, O. Lupan, T. Braniste, V. Duppel, I. Tiginyanu, L. Kienle, R. Adelung and Y. K. Mishra, *Advanced Electronic Materials*, 2015, **1**.
10. S. Mao, S. Cui, G. Lu, K. Yu, Z. Wen and J. Chen, *Journal of Materials Chemistry*, 2012, **22**.
11. J. H. Kim, A. Katoch, H. W. Kim and S. S. Kim, *Chem Commun (Camb)*, 2016, **52**, 3832-3835.
12. J. L. Johnson, A. Behnam, S. J. Pearton and A. Ural, *Adv Mater*, 2010, **22**, 4877-4880.
13. X. Q. Zeng, M. L. Latimer, Z. L. Xiao, S. Panuganti, U. Welp, W. K. Kwok and T. Xu, *Nano Lett*, 2011, **11**, 262-268.
14. W. T. Koo, S. Qiao, A. F. Ogata, G. Jha, J. S. Jang, V. T. Chen, I. D. Kim and R. M. Penner, *ACS Nano*, 2017, **11**, 9276-9285.
15. Y. T. Pan, X. Yin, K. S. Kwok and H. Yang, *Nano Lett*, 2014, **14**, 5953-5959.
16. J. Hong, S. Lee, J. Seo, S. Pyo, J. Kim and T. Lee, *ACS Appl Mater Interfaces*, 2015, **7**, 3554-3561.
17. P. A. Russo, N. Donato, S. G. Leonardi, S. Baek, D. E. Conte, G. Neri and N. Pinna, *Angew Chem Int Ed Engl*, 2012, **51**, 11053-11057.
18. A. A. Haidry, A. Ebach-Stahl and B. Saruhan, *Sensors and Actuators B: Chemical*, 2017, **253**, 1043-1054.
19. Y. Wang, Z. Zhao, Y. Sun, P. Li, J. Ji, Y. Chen, W. Zhang and J. Hu, *Sensors and Actuators B: Chemical*, 2017, **240**, 664-673.
20. X. Li, X. Zhou, H. Guo, C. Wang, J. Liu, P. Sun, F. Liu and G. Lu, *ACS Appl Mater Interfaces*, 2014, **6**, 18661-18667.
21. A. Katoch, J.-H. Byun, S.-W. Choi and S. S. Kim, *Sensors and Actuators B: Chemical*, 2014, **202**, 38-45.
22. A. Cabot, J. Arbiol, J. R. Morante, U. Weimar, N. Barsan and W. Gopel, *Sensor Actuat B-Chem*, 2000, **70**, 87-100.
23. M. Hubner, D. Koziej, J. D. Grunwaldt, U. Weimar and N. Barsan, *Phys Chem Chem Phys*, 2012, **14**, 13249-13254.
24. C.-T. Wang, H.-Y. Chen and Y.-C. Chen, *Sensors and Actuators B: Chemical*, 2013, **176**, 945-951.
25. G. Korotcenkov, V. Brinzari, L. B. Gulina and B. K. Cho, *Applied Surface Science*, 2015, **353**, 793-803.
26. R. Peng, Y. Li, T. Liu, Q. Sun, P. Si, L. Zhang and L. Ci, *Chem Phys Lett*, 2019, **737**.
27. J. B. Chang, H. H. Pu, S. A. Wells, K. Y. Shi, X. R. Guo, G. H. Zhou, X. Y. Sui, R. Ren, S. Mao, Y. T. Chen, M. C. Hersam and J. H. Chen, *Mol Syst Des Eng*, 2019, **4**, 491-502.
28. Z. Wang, Y. Zhang, S. Liu and T. Zhang, *Sensors and Actuators B: Chemical*, 2016, **222**, 893-903.

29. L. Wang, D. Wang, Z. Dong, F. Zhang and J. Jin, *Nano Lett*, 2013, **13**, 1711-1716.
30. S. Wang, Y. Zhao, J. Huang, Y. Wang, H. Ren, S. Wu, S. Zhang and W. Huang, *Applied Surface Science*, 2007, **253**, 3057-3061.
31. S. Pei and H.-M. Cheng, *Carbon*, 2012, **50**, 3210-3228.
32. A. Venkatesan, S. Rathi, I. Y. Lee, J. Park, D. Lim, M. Kang, H. I. Joh, G. H. Kim and E. S. Kannan, *Nanotechnology*, 2017, **28**, 365501.
33. V. Palmisano, E. Weidner, L. Boon-Brett, C. Bonato, F. Harskamp, P. Moretto, M. B. Post, R. Burgess, C. Rivkin and W. J. Buttner, *International Journal of Hydrogen Energy*, 2015, **40**, 11740-11747.
34. T. Hübert, L. Boon-Brett, G. Black and U. Banach, *Sensors and Actuators B: Chemical*, 2011, **157**, 329-352.
35. B. Ruhland, T. Becker and G. Muller, *Sensor Actuat B-Chem*, 1998, **50**, 85-94.
36. S. M. Cui, H. H. Pu, G. H. Lu, Z. H. Wen, E. C. Mattson, C. Hirschmugl, M. Gajdardziska-Josifovska, M. Weinert and J. H. Chen, *Acs Appl Mater Inter*, 2012, **4**, 4898-4904.
37. D. Zhang, Y. e. Sun, C. Jiang and Y. Zhang, *Sensors and Actuators B: Chemical*, 2017, **242**, 15-24.
38. A. S. N. Asama N. Naje, Abdulla M. Suhail, *Int. J. Innov. Res. Sci. Eng. Technol*, 2013, **12**, 7068-7072.
39. Z. Bo, M. Yuan, S. Mao, X. Chen, J. Yan and K. Cen, *Sensors and Actuators B: Chemical*, 2018, **256**, 1011-1020.
40. G. Lu, L. E. Ocola and J. Chen, *Advanced Materials*, 2009, **21**, 2487-2491.
41. D. Degler, S. Rank, S. Müller, H. W. Pereira de Carvalho, J.-D. Grunwaldt, U. Weimar and N. Barsan, *ACS Sensors*, 2016, **1**, 1322-1329.
42. J. D. Fowler, M. J. Allen, V. C. Tung, Y. Yang, R. B. Kaner and B. H. Weiller, *ACS Nano*, 2009, **3**, 301-306.
43. F. A. A. Nugroho, I. Darmadi, L. Cusinato, A. Susarrey-Arce, H. Schreuders, L. J. Bannenberg, A. B. da Silva Fanta, S. Kadkhodazadeh, J. B. Wagner, T. J. Antosiewicz, A. Hellman, V. P. Zhdanov, B. Dam and C. Langhammer, *Nat Mater*, 2019, **18**, 489-495.